Estimating global black carbon emissions using a top-down Kalman Filter approach*

Jason Blake Cohen and Chien Wang

MIT JOINT PROGRAM ON THE SCIENCE AND POLICY of GLOBAL CHANGE

***Reprinted from**
***Journal of Geophysical Research—Atmospheres*, 119: 1–17**
doi: 10.1002/2013JD019912
Copyright © 2014 with kind permission from the authors

Reprint 2014-1

The MIT Joint Program on the Science and Policy of Global Change combines cutting-edge scientific research with independent policy analysis to provide a solid foundation for the public and private decisions needed to mitigate and adapt to unavoidable global environmental changes. Being data-driven, the Program uses extensive Earth system and economic data and models to produce quantitative analysis and predictions of the risks of climate change and the challenges of limiting human influence on the environment—essential knowledge for the international dialogue toward a global response to climate change.

To this end, the Program brings together an interdisciplinary group from two established MIT research centers: the Center for Global Change Science (CGCS) and the Center for Energy and Environmental Policy Research (CEEPR). These two centers—along with collaborators from the Marine Biology Laboratory (MBL) at Woods Hole and short- and long-term visitors—provide the united vision needed to solve global challenges.

At the heart of much of the Program's work lies MIT's Integrated Global System Model. Through this integrated model, the Program seeks to: discover new interactions among natural and human climate system components; objectively assess uncertainty in economic and climate projections; critically and quantitatively analyze environmental management and policy proposals; understand complex connections among the many forces that will shape our future; and improve methods to model, monitor and verify greenhouse gas emissions and climatic impacts.

This reprint is one of a series intended to communicate research results and improve public understanding of global environment and energy challenges, thereby contributing to informed debate about climate change and the economic and social implications of policy alternatives.

Ronald G. Prinn and John M. Reilly,
Program Co-Directors

For more information, contact the Program office:

MIT Joint Program on the Science and Policy of Global Change
Postal Address:
Massachusetts Institute of Technology
77 Massachusetts Avenue, E19-411
Cambridge, MA 02139 (USA)
Location:
Building E19, Room 411
400 Main Street, Cambridge
Access:
Tel: (617) 253-7492
Fax: (617) 253-9845
Email: ***globalchange@mit.edu***
Website: ***http://globalchange.mit.edu/***

Estimating global black carbon emissions using a top-down Kalman Filter approach

Jason Blake Cohen[1,2] and Chien Wang[1,3]

Received 28 March 2013; revised 14 October 2013; accepted 16 October 2013.

[1] Black carbon (BC) is an important aerosol constituent in the atmosphere and climate forcer. A good understanding of the radiative forcing of BC and associated climate feedback and response is critical to minimize the uncertainty in predicting current and future climate influenced by anthropogenic aerosols. One reason for this uncertainty is that current emission inventories of BC are mostly obtained from the so-called bottom-up approach, an approach that derives emissions based on categorized emitting sources and emission factors used to convert burning mass to emissions. In this work, we provide a first global-scale top-down estimation of global BC emissions, as well as an estimated error range, by using a Kalman Filter. This method uses data of both column aerosol absorption optical depth and surface concentrations from global and regional networks to constrain our fully coupled climate-aerosol-urban model and thus to derive an optimized estimate of BC emissions as 17.8 ± 5.6 Tg/yr, a factor of more than 2 higher than commonly used global BC emissions data sets. We further perform 22 additional optimization simulations that incorporate the known uncertain ranges of various important physical, model, and measurement parameters and still yield an optimized value within the above given range, from a low of 14.6 Tg/yr to a high of 22.2 Tg/yr. Furthermore, we show that the emissions difference between our optimized and a priori estimation is not uniform, with East Asia, Southeast Asia, and Eastern Europe underestimated, while North America is overestimated in the a priori inventory.

Citation: Cohen, J. B., and C. Wang (2014), Estimating global black carbon emissions using a top-down Kalman Filter approach, *J. Geophys. Res. Atmos.*, *119*, doi:10.1002/2013JD019912.

1. Introduction

[2] Black carbon (BC) is produced due to incomplete combustion of carbon-containing substances: fossil fuels, biofuels, forest and agricultural fires, and other combustion-related processes. BC is important with respect to both air quality and the global climate system; it is a component of particulate matter and is one of the only few species that uniquely interacts with solar radiation through both scattering and absorption. Interactions of BC with solar radiation lead to changes in the net energy budget of the Earth. At the top of the atmosphere, estimated global radiative forcing of BC covers a broad range of values as computed by a range of models using many different assumptions, though all positive (i.e., a net warming), ranging from low to high, which includes the following: 0.25 ± 0.15 [*Forster et al.*, 2007], 0.26 [*Kim et al.*, 2008], 0.35 [*Wang*, 2004; *Cohen et al.*, 2011], 0.53 [*Ming et al.*, 2010], 0.6 [*Chung and Seinfeld*, 2005], 0.62 [*Jacobson*, 2001], and 0.9 [*Ramanathan and Carmichael*, 2008] W/m^2. BC has been shown to directly heat the atmosphere through its strong absorption of visible sunlight (unlike many other aerosol species which do not absorb visible radiation). Additionally, both scattering and absorbing extinction of sunlight by BC lead to a reduction of solar radiation at the surface, or a net cooling, impacting the general surface energy budget and thus the surface evapotranspiration as well as temperature. The atmospheric heating and surface cooling by BC, either acting alone or together, have been demonstrated to change large-scale circulation and precipitation patterns [e.g., *Satheesh and Ramanathan*, 2000; *Ramanathan et al.*, 2001; *Chung and Ramanathan*, 2003; *Wang*, 2004; *Ramanathan et al.*, 2005; *Wang*, 2009].

[3] Presently, the global-scale emissions of aerosols (including BC) are computed primarily based on various bottom-up methods [*Bond et al.*, 2004; *Sokolov et al.*, 2009; *Zhang et al.*, 2009; *Lei et al.*, 2011; *Jacobson*, 2012]. What these various methods include are measures of economic and natural activities leading to the production of BC, measures of the population and quantities of substances leading to BC emissions, and quantification of the yield of BC from each unit of activity. Estimations based on these bottom-up

[1]Center for Environmental Sensing and Modeling, Singapore-MIT Alliance for Research and Technology Center, Singapore, Singapore.
[2]Now at Department of Civil and Environmental Engineering, National University of Singapore, Singapore, Singapore.
[3]Center for Global Change Science, Massachusetts Institute of Technology, Cambridge, Massachusetts, USA.

Corresponding author: J. B. Cohen, Department of Civil and Environmental Engineering, National University of Singapore, 1 Engineering Drive 2, E1A-07-03, Singapore 117576, Singapore. (ceecjb@nus.edu.sg)

©2013. The Authors.
This is an open access article under the terms of the Creative Commons Attribution-NonCommercial-NoDerivs License, which permits use and distribution in any medium, provided the original work is properly cited, the use is non-commercial and no modifications or adaptations are made.
2169-897X/14/10.1002/2013JD019912

methods provide much needed information from spatial distributions to emission rates of BC around the globe. However, most of the economic indicators used in these derivations are coarsely modeled or measured, the population and quantities are often estimated from small samples, or interpolated with assumptions where data does not exist, and the measurements of BC production from activities are estimated either based on idealized laboratory conditions or only from a small sample of field experiments. Each stage in the above described procedure introduces errors of aggregation, extrapolation, or expert opinion, leading to large uncertainties associated with the outcomes of this approach.

[4] The loadings of BC are heterogeneously distributed over the surface of the Earth, varying by more than an order of magnitude. This is due in part to widely varying emission sources in space and time. For example, although cities and open fires only cover a very small area of the Earth's surface, they contribute much of the total emissions. The states of the emissions from both are also hard to predict, due to the dynamic nature of city development and randomness in fire events, contributing further to BC emission uncertainty. Second, the major removal mechanism of BC in the atmosphere is wet deposition, which, despite varying in space and time, is a process generally leading to an average lifetime of BC of about a week and thus limiting the transport distance of BC from source regions. Given the heterogeneous nature of rainfall, this also would lead to a variable BC field, even if the emissions sources were uniform. The concept of wet deposition includes two components, i.e., the nucleation scavenging that activates aerosols and forms cloud droplets or ice crystals and the impact scavenging that collects aerosols during the fall of precipitating cloud drops. Since BC tends to be more hydrophobic than other aerosols, the nucleation scavenging of BC is believed to differ from other types of more hydroscopic aerosols unless it is coated with water-soluble materials [cf. *Tao et al*., 2012]. Because of these properties, BC, unless it is coated, is even regarded as ineffective for ice nuclei as well [e.g., *Hoose and Möhler*, 2012].

[5] Here we report a new estimation of the global amount of BC emissions from a completely different perspective, using a top-down estimation technique called the Kalman Filter [*Kalman*, 1960; *Sorenson*, 1970; *Enting*, 2002; *Prinn*, 2004]. While this provides us with new insight and a constraint on the emissions of BC, neither this approach nor the bottom-up approach alone is sufficient to provide an exact answer. The reason for this is that the top-down approach still relies on the bottom-up spatial a priori assumptions. Nevertheless, combining top-down and bottom-up approaches is still expected to provide improved estimation because of the use of multiple constraints and complementary methods.

[6] There were previous efforts using different top-down techniques to estimate BC emissions. Some of these were applied to specific geographical regions rather than covering the whole globe [*Tarantola and Valette*, 1982; *Hakami et al*., 2005; *Yongtao et al*., 2009; *Kondo et al*., 2011]. Other efforts have been applied to specific types of burning sources and geographical regions, such as biomass burning, over a specific limited time frame [*Zhang et al*., 2005]. Others still have been based on a simple linear scaling of concentration [*Sato et al*., 2003; *Wang et al*., 2011]. However, ours is the first known use of the Kalman Filter technique and the first to optimize for the annual average global emissions of BC.

[7] In this paper, we first describe our method and data in detail and compare alternative approaches (sections 2.1, 2.2, and 2.3). We then present the result of our optimization of global BC emissions (sections 2.4 and 3.1) as well as analysis on optimized emissions in comparison with corresponding a priori over several important regions (section 3.2). This is followed by the further discussions of the results and conclusions (section 4).

2. Methodological Framework Used in This Study

2.1. Observational Data

[8] The backbone of a global top-down technique is using a set of observational constraints that sufficiently sample the span of Earth's surface and atmosphere, sufficient to obtain information on a variable at the global scale. In this study, observations of column absorption, surface concentration, and near-surface local absorption from several global or continental networks have been used. The data used are monthly average values and the standard deviation of the daily average values that were used to produce the monthly averages. The data cover the 8 year period of time from January 2002 through December 2009. Overall, 112 stations from the Aerosol Robotic Network (AERONET) [*Holben et al*., 1998], 8 surface measurement stations from the European Supersites for Atmospheric Aerosol Research (EUSAAR) network [*Cavalli et al*., 2010], 14 surface measurement stations from the Chinese Atmosphere Watch Network (CAWNET) [*Zhang et al*., 2012], and 4 surface measurement stations from the NOAA Earth System Research Laboratory/Global Monitoring Division Network (NOAA) [*Delene and Ogren*, 2002] are included. A map of the locations of the various stations is given in Figure 1.

[9] In summary, there are three different types of measurements compared against corresponding modeled values: column aerosol absorbing optical depth (AAOD), surface AAOD, and surface concentration of total BC (the sum of pure BC and the BC component of core-shell mixed BC). The AERONET measurements provide a measure of the total column aerosol optical depth (AOD) and an approximation of the column single-scatter albedo (SSA) ω, the scattering fraction in total sunlight extinction. Both quantities are dimensionless. Since there are known issues with AERONET not being able to compute ω correctly at low AOD values, only data corresponding to an AOD greater than 0.4 were included for the main inversion [*Dubovik et al*., 2000]. For the purpose of the main analysis, we only use stations that have no more than 30% of their data points under this 0.4 limit. This assumption is further tested and detailed by sensitivity runs (each of which requires a full and entire rerun of the modeling system) in a later section. The AAOD, a measure of the total column absorbance due to all absorbing aerosols, is derived by

$$\mathrm{AAOD} = \mathrm{AOD} * (1 - \omega) \tag{1}$$

[10] The surface measurements reported from the NOAA network were given as σ_{abs} (m^{-1}). This measurement value can be mapped to an AAOD value by dividing the surface layer component of the AAOD by the height of the surface layer Z_{surf} (for models this is approximately 50 m):

$$\mathrm{AAOD}_{\mathrm{surf,model}}/Z_{\mathrm{surf,model}} = \sigma_{\mathrm{abs,model}} \tag{2}$$

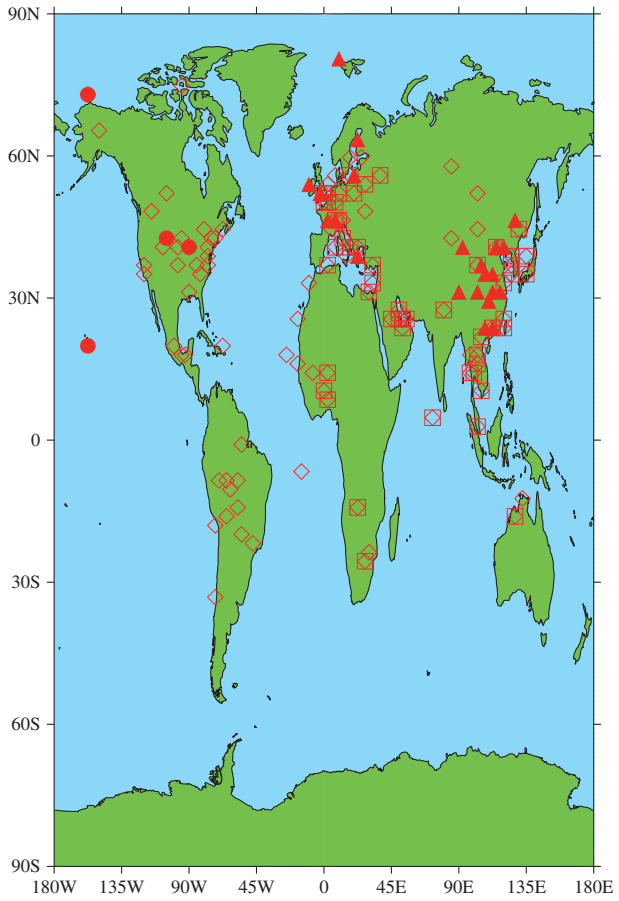

Figure 1. Locations of the various measurement devices used for the inversion. While all AERONET stations are given as open diamonds, the fraction used in Case 10 also has a rectangle over the diamond. Surface concentration stations (EUSAAR and CAWNET) are given by filled triangles, while surface absorption stations (NOAA) are given by filled circles.

[11] The surface measurements reported from both EUSAAR network and CAWNET were given as concentration of BC based on aethalometer measurements and therefore are directly compared with modeled surface concentrations of BC.

[12] Many of the AERONET stations over North America report regularly measured AOD that falls below 0.4 and thus cannot provide an AAOD retrieval for these regions. However, a constraint of the emissions from North America can still be obtained based on a subset of North American AERONET stations, as well as those measuring the flow of material from North America, which do not suffer from this same issue. This subset specifically includes the following stations: two Mexican Urban areas, three metro U.S. areas (New York City, Los Angeles, and Washington DC), one metro area in Canada (Toronto), Puerto Rico, and even a few stations situated in Southwestern Europe and Northwestern Africa. The surface data from NOAA stations also help to fill the gap, providing an additional constraint in our approach. The CAWNET and EUSAAR data similarly provide complementary constraints over both Europe and East Asia, helping to fill in gaps in regions over where there are no AERONET stations or the AERONET stations do not regularly report AOD exceeding the 0.4 cutoff. This is important since Eastern Europe and East Asia only have partial coverage by AERONET stations, yet both are significant source regions of BC.

[13] Column AAOD data include contributions from three species: BC, dust, and absorbing organic carbon (OC), and therefore, further work has to be done to extract the BC component, as shown in equation (3):

$$\mathrm{AAOD_{BC}} = \mathrm{AAOD_{Measured}} - \mathrm{AAOD_{dust}} - \mathrm{AAOD_{OC}} \quad (3)$$

[14] The monthly dust climatology derived by *Mahowald et al.* [2003] with a correction to the fine fraction optical properties has been used to compute the AAOD associated with dust. This is an important factor contributing significantly to the total AAOD at different stations located in regions close to and downwind from large dust sources while not contributing at all to the AAOD at stations far away from dust sources, as found both in the data used for this paper as well as by *Wang et al.* [2009]. To address the contribution of OC to the AAOD, the model-derived value of the AAOD from OC, which accounts for between 2.9% and 3.2% of the total AAOD, is also used. We make these computations by assuming that the AAOD value calculated by considering the internal mixtures of BC with dust and those of BC with OC would not be substantially different than those calculated by combining the individual AAOD values derived from each of these involved constituents separately. This allows the measured representation of BC to be obtained through simple subtraction, as given in equation (3). Since the assumption of the magnitude of the AAOD associated with dust is uncertain, a couple of tests will address this issue in the sensitivity runs section.

[15] To properly construct a full time series over the entire 8 years spanned, missing data points were interpolated. This was done by first computing the month-by-month climatological average over the period from 2002 to 2010 and by using this value to fill in any missing points. If there were no data available for a given month, then a linear interpolation was used between the two closest points, in time, having actual data. The data, aggregated by region, are given in Figure 2.

[16] The end result is the values of the various measurements in an ordered array that can be directly compared with the model. To achieve this mathematically, the measurements and their associated errors will need to be arranged into a single time-varying vector. Such an observation vector can be defined as $\mathbf{y^o}_k$, where k is the index reflecting the time step (in this case monthly). The first 112 terms respectively of $\mathbf{y^o}_k$ for each given time k are the AAODs associated with BC derived from 112 AERONET stations. The next 22 terms of $\mathbf{y^o}_k$ for each given time k are the direct BC measurements from the 8 EUSAAR and 14 CAWNET surface stations, respectively, given in terms of concentration ($\mu g/m^3$). The last 4 terms of $\mathbf{y^o}_k$ for each given time k are the measurements of $\mathrm{AAOD_{surf}}$ from NOAA stations. This yields a time-varying observation vector $\mathbf{y^o}_k$ having a length of 138.

[17] A similar observation error vector $\boldsymbol{\varepsilon}_k$ is also formed. The standard deviation of the underlying daily average values that were used to compute the monthly average values in $\mathbf{y^o}_k$ were used to represent the observation error vector $\boldsymbol{\varepsilon}_k$. For points with missing data in $\mathbf{y^o}_k$, the values were either climatologically averaged or interpolated, and hence, no

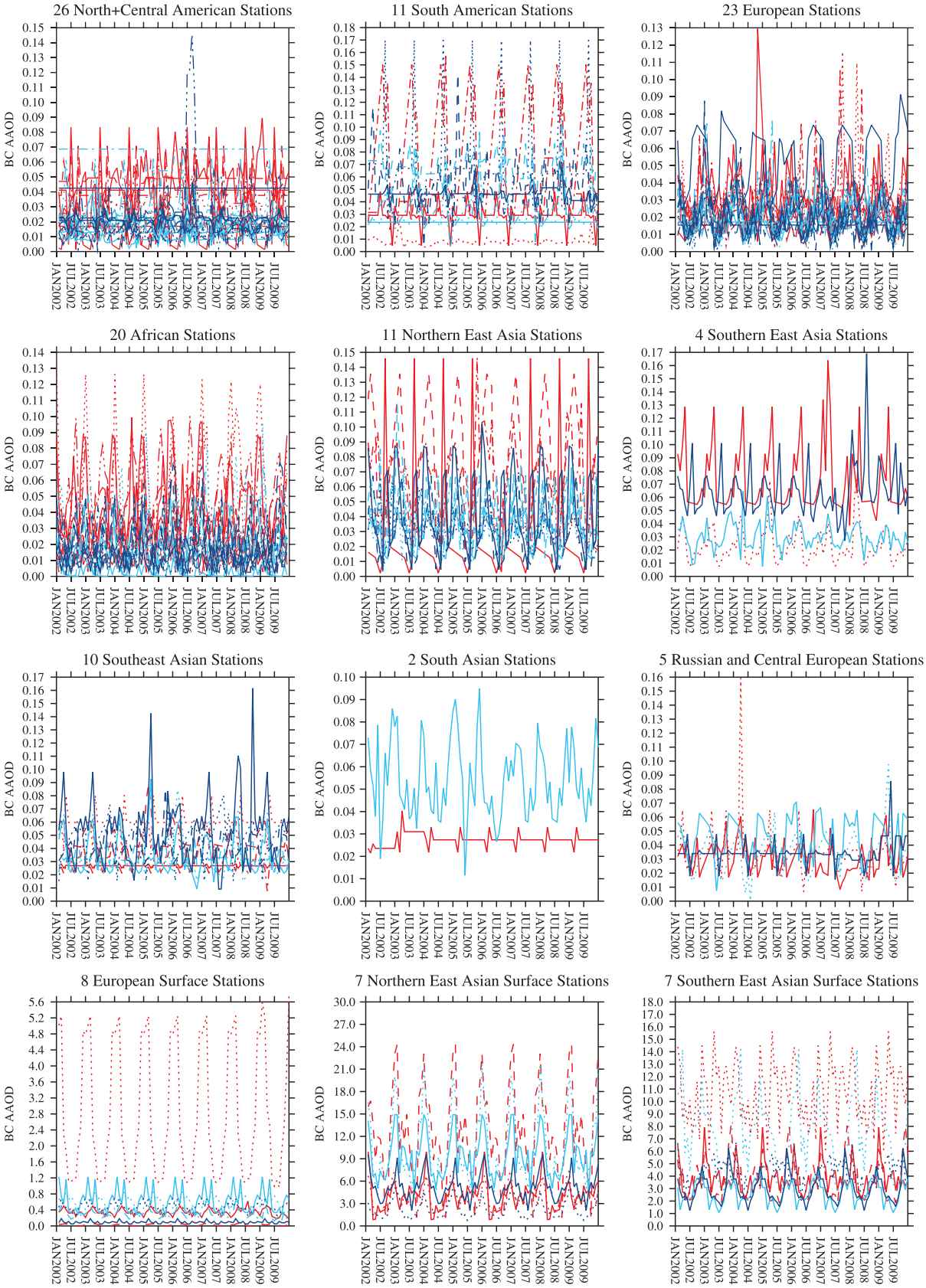

Figure 2. Monthly averaged data from AERONET $AAOD_{BC}$ (as per equation (3)) and EUSAAR and CAWNET surface BC ($\mu g/m^3$) for each of the sites used in the inversion. Each line corresponds to the data from one site, from 2002–2010. The individual lines also include those points that have been interpolated, as explained in the text. The different panels show the data grouped by corresponding region (see Figure 4).

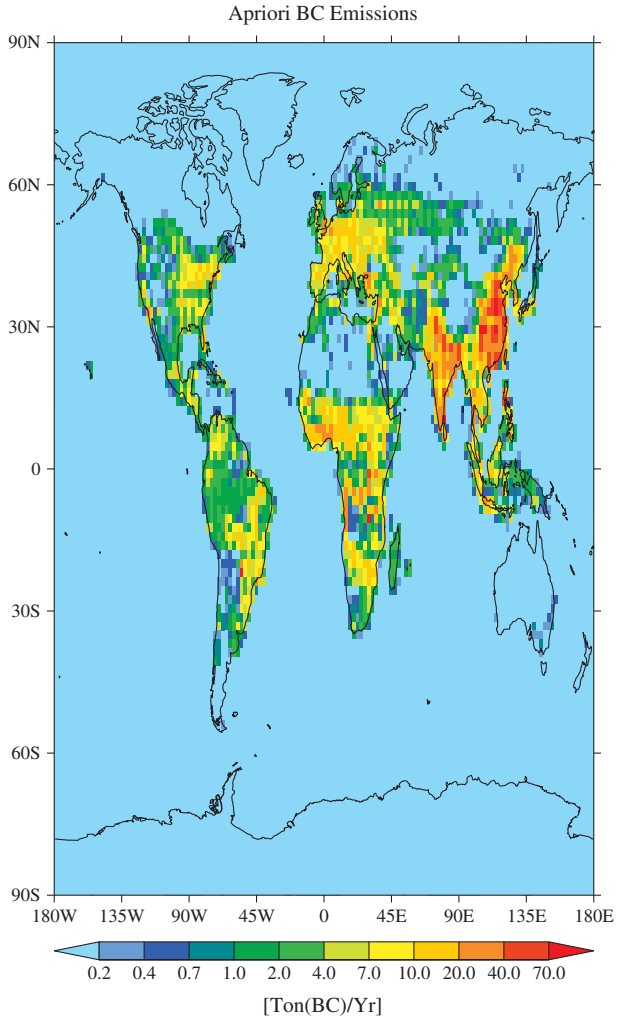

Figure 3. A priori BC emissions.

standard observation error can be computed. In these cases, the standard deviation was set to be the same as the value itself of $\mathbf{y^o}_k$, assuring that they will not contribute to the overall solution. Furthermore, there is a fundamental uncertainty associated with the measurements themselves, and this provides an additional constraint on $\boldsymbol{\varepsilon}_k$. Since the errors associated with the absorption inversion tend to be at least 15% [*Dubovik et al*., 2000; *Schuster et al*., 2005], the minimum allowable error for each term $\boldsymbol{\varepsilon}_k$ is set to be $0.15\,\mathbf{y^o}_k$. The point of these decisions is to make sure that interpolated data points have little weight on the final inversion and that measurement error is fairly represented as being the greater of the variation in the monthly average and the error associated with the equipment and algorithms themselves. These assumptions are further tested in the sensitivity runs section.

2.2. Models

[18] The other component for performing the inversion is a suitable global model that can simulate values of BC AAOD and BC surface concentration that correspond with the respective measurements of BC AAOD and BC surface concentration (vectors $\mathbf{y^o}_k$ and $\boldsymbol{\varepsilon}_k$) at the same location and time. For this work, we have chosen to use the MIT AERO-URBAN model [*Kim et al*., 2008; *Cohen et al*., 2011], a state-of-the-art modeling system that simulates the chemistry and transport at regional to global scales. The model includes a 3-D general circulation model derived from the Community Atmospheric Model (CAM) version 3.1 [*Collins et al*., 2006]. The dynamical core is coupled with a treatment of aerosol physics, chemistry, and radiation interactions, including a two-moment representation of each of the seven anthropogenic aerosol types and time-varying emissions of secondary organic aerosol [*Kim et al*., 2008]. Furthermore, both the aerosol and dynamical modules are interconnected with a metamodel of urban-scale processing of aerosols and their precursors. This metamodel computes the quantitative impact of nonlinear urban-scale chemical and physical processing on aerosols, allowing for this to be taken into consideration even though the model is of global spatial and temporal resolution [*Cohen et al*., 2011; *Cohen and Prinn*, 2011].

[19] For this specific experiment, the model was used in its atmospheric transport model mode, driven by National Center for Environment Prediction reanalysis fields at a 6-hourly time resolution [*Kalnay et al*., 1996]. In terms of dynamical fields, the precipitation, vertical velocity, and cumulus mass flux fields, along with many others, are computed by CAM. A full list of which fields are computed by CAM and which are used from reanalysis can be found in *Cohen et al*. [2011] and other references therein. The important contributions of the aerosol model as applied to this study include three factors that contribute to the unique representation of both the AAOD associated with BC and OC and the surface BC concentration fields, all on the global scale. First, that the radiative calculations are based on the trio of external modes of BC and OC, a core-shell representation of BC and sulfate (MBS), and an internal mixture of OC and sulfate (MOS). Second, that a minimum concentration of sulfuric acid is required before aging of BC or OC can occur. Third, the aerosol processing includes the coupling of an urban-scale processing model, which takes into account the nonlinearity in chemistry, physics, and scavenging of aerosols and their precursors that occur in these high-concentration regimes, which tend to lead to a reduction in SO_2, more aging of the particles, and a higher number concentration of smaller particles around and downwind from urban areas. In all, these lead to the computation of a set of global-scale fields of BC and MBS, which in turn are used to derive AAOD and mass concentrations of BC, while fields of OC and MOS are used to derive the AAOD associated with OC.

2.3. Kalman Filter

[20] The top-down estimation performed here is done using a Kalman Filter technique. Although this technique has been used extensively for atmospheric trace gases [*Mahowald et al*., 1997; *Prinn et al*., 2001; *Chen and Prinn*, 2006], it has not yet been applied to aerosol-related problems on a global scale. Much of the underlying mathematical representation is described in works by *Enting* [2002] and *Prinn* [2004].

[21] Since the forward model is run at $1.9° \times 2.5°$ resolution, the inverse problem is ill posed and cannot be solved for each grid point, given that there are only 138 total data points at each time step, yet there are over 2000 underlying grid points that contain emissions. The a priori emissions, given in Figure 3, are distributed based on underlying

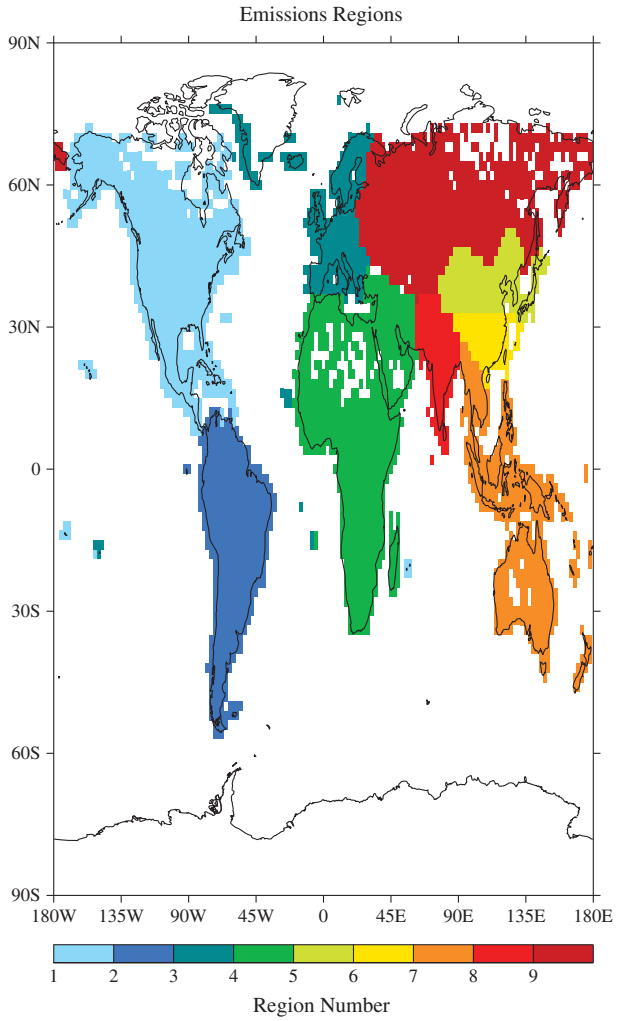

Figure 4. Nine geospatially defined regions used in this inversion.

economic activity, population, and geographical regions of the world [*Kim et al.*, 2008; *Cohen et al.*, 2011]. Therefore, to make the problem tractable, the a priori emissions distributed over the globe have been aggregated spatially into nine unique regions. Each region retains its distinct spatial characteristics of emissions and is scaled up or down as a unit. These regions were chosen such that they were tiled over Earth's surface in such a way that they are orthogonal to each other, as shown in Figure 4, with the names of each of these regions also concurrently given in Table 1. This specifically means that not only the tiles corresponding to the emissions are unique but also that the emitted BC from these regions, after transport and processing have occurred, retains a particular spatial and temporal distribution of both AAOD and BC surface concentration values.

[22] Although orthogonality of the regions is required for the Kalman Filter equations to be mathematically precise, obtaining this in the physical world is not strictly possible. To approximate this as best as possible, these nine separate spatial regions were chosen such that each encompasses a sizeable amount of the total BC emissions. Furthermore, these regions were chosen such that their emissions interact with the general circulation and chemical and physical processes in the atmosphere in as unique a manner as possible. Also, to keep the Kalman Filter numerics stable, each region has been chosen so that its emissions and sensitivity to detection from the different measurement sites are roughly equal (in an order of magnitude sense). This allows the matrix to not be ill conditioned, allowing for fewer numerical issues during the matrix inversion step.

[23] The model, which has a time step of 30 min, is integrated forward, and the average monthly values are then used to compute the sensitivity of how a change in emissions of BC from any given region impacts on the model value mapped to $\mathbf{y}^{\mathbf{o}}{}_k$ and $\boldsymbol{\varepsilon}_k$ at each model location where a measurement exists. This sensitivity matrix, $\mathbf{H}_{ijk}$ has dimensionality of i by j for each given time step k and is defined by equation (4a).

$$\mathbf{H}_{ijk} = \mathrm{d}\mathbf{y}_{ik}/\mathrm{d}\mathbf{x}_{jk} \tag{4a}$$

[24] As can be seen, the sensitivity matrix relates how a change in the BC emissions from any given region $j = (1\ldots 9)$ at any time k, $\mathbf{x}_{jk}$, quantitatively relates to a change in the given respective model value (AAOD, surface concentration, or surface AAOD), $\mathbf{y}_{ik}$, at the same spatial location corresponding to each measurement location $i = (1\ldots 138)$ given by $\mathbf{y}^{\mathbf{o}}{}_k$ at each monthly time step k. Specifically, this perturbation is applied equally in each region for all k months that the model is run.

[25] To calculate equation (4a), further assumptions are required. The first is to assume that the sensitivity matrix components behave roughly linearly for small changes in emissions (due to BC lifetime and spatial locations of stations within model grid boxes). This allows the underlying model to be run a total of 10 times, one with the a priori emissions and nine more as perturbations cases. Each perturbation case $j = (1,\ldots,9)$ is identical to the a priori case with the exception that the emissions for a given single region j are increased by a uniformly distributed constant amount of 0.2 Tg/year. In this way, the underlying model values corresponding to $\mathbf{y}_{ik}$ are approximated for the a priori case and each of the perturbation cases j, at each point and for each time step. All of this computation is based on the monthly varying meteorology, concentrations, chemistry, and physics. Then the terms of the sensitivity matrix given in equation (4a) can be approximated by the first-order difference, as shown in equation (4b):

$$\mathbf{H}_{ijk} \approx \left(\mathbf{y}_{ik-\mathrm{pert}} - \mathbf{y}_{ik\ -\ \mathrm{base}}\right) / \left(\mathbf{x}_{jk-\mathrm{pert}} - \mathbf{x}_{jk-\mathrm{base}}\right) \tag{4b}$$

[26] Here the subscript "pert" and "base" represent the perturbation case j and base case, respectively. The values of the sensitivity matrix for the 20 stations for each of the 9 regions j

Table 1. Name List of Corresponding Regions as Given in Figure 4 and Used in Tables 2 and 3

Region Number	Region Name
1	North and Central America
2	South America
3	Europe
4	Africa and Middle East
5	Northern East Asia
6	Southern East Asia
7	Southeast Asia and Australia
8	South Asia
9	Russia and Eastern Europe

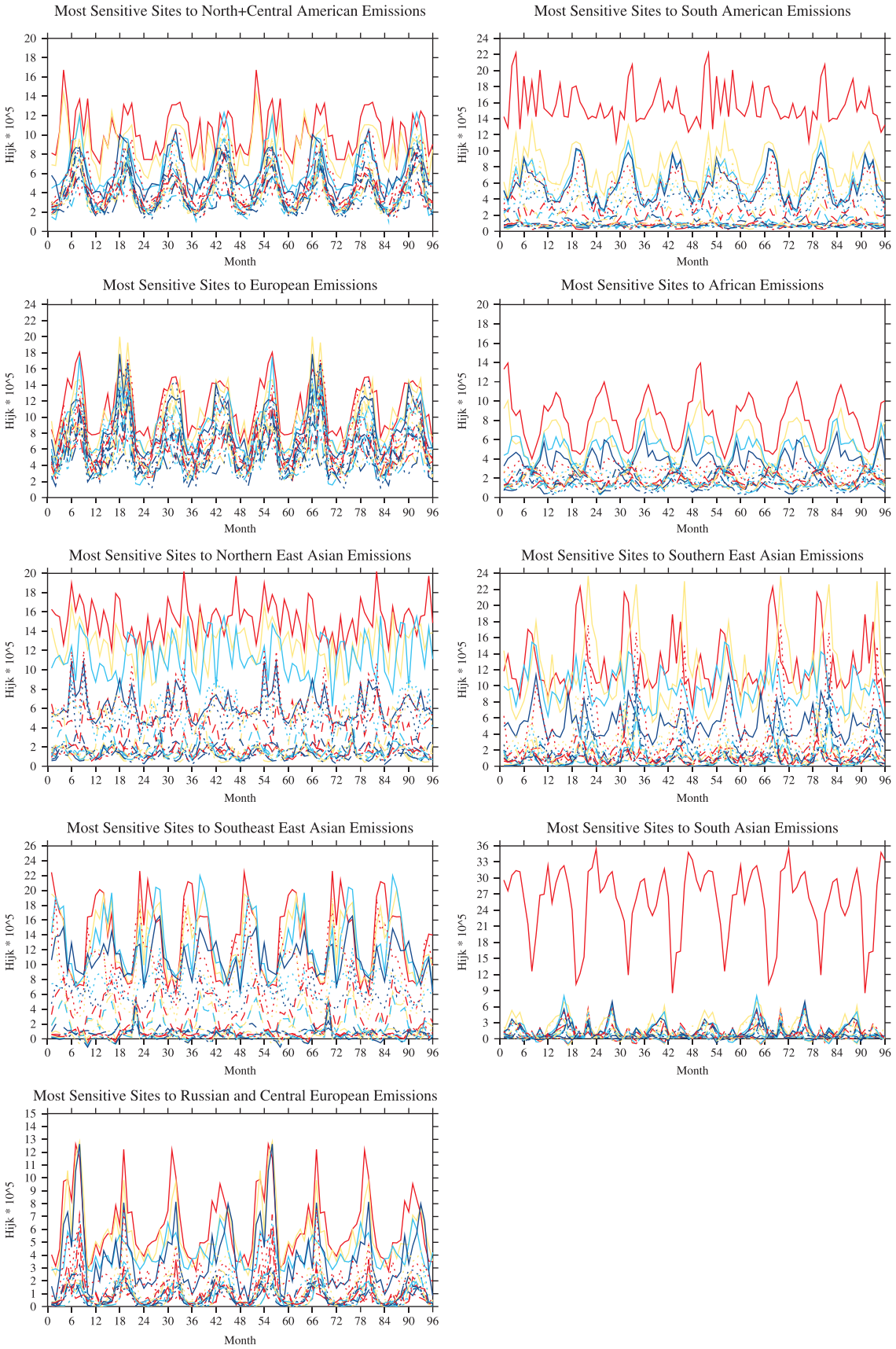

Figure 5. Time series plots of the 20 sites contributing the largest average amount to the sensitivity matrix $\mathbf{H}_{ijk}$ (see equations (4a) and (4b)). These are plotted for the sensitivity over each of the nine regions (see Figure 4) used in the base inversion calculation.

Table 2. Definitions of the Base Case and Various Sensitivity Cases Used for Testing the Optimization Under Different Model, Measurement, and Filter Assumptions[a]

	Emissions $\Sigma(\mathbf{x}_{jk,0})$ (Tg/yr)	Interpolation Error $\varepsilon_k = \mathrm{Xx}\mathbf{y^o}_k$	Model Error $\mathbf{Q}_k = \mathrm{XX}\mathbf{P}_k$	Aeronet Data	Optical Properties
Base	14	1.0	0.1	AOD > 0.4	Base
		Differences in a Priori *Emissions*			
Case 1	(8)	1.0	0.1	AOD > 0.4	Base
Case 2	(17)	1.0	0.1	AOD > 0.4	Base
Case 3	(20)	1.0	0.1	AOD > 0.4	Base
		Differences in Interpolation Error			
Case 4	14	(2.0)	0.1	AOD > 0.4	Base
Case 5	(8)	(2.0)	0.1	AOD > 0.4	Base
Case 6	(17)	(2.0)	0.1	AOD > 0.4	Base
Case 7	(20)	(2.0)	0.1	AOD > 0.4	Base
		Differences in Model Error			
Case 8	14	1.0	(0.00)	AOD > 0.4	Base
Case 9	14	1.0	(0.05)	AOD > 0.4	Base
Case 10	14	1.0	(0.15)	AOD > 0.4	Base
Case 11	14	1.0	(0.20)	AOD > 0.4	Base
		Differences in the AERONET Cutoff			
Case 12	14	1.0	0.10	(20% Filter)	Base
Case 13	14	1.0	0.10	(All data)	Base
		Differences in SSA Assumptions of MBS			
Case 14	14	1.0	0.10	AOD > 0.4	(High SSA)
Case 15	14	1.0	0.10	AOD > 0.4	(Low SSA)
		Differences in BC Density			
Case 16	14	1.0	0.10	AOD > 0.4	(High ρ)
Case 17	14	1.0	0.10	AOD > 0.4	(Low ρ)
		Differences Using a Much Higher BC Density			
Case 18	14	1.0	0.10	AOD > 0.4	($\rho = 1.5$)
Case 19	14	1.0	0.10	AOD > 0.4	($\rho = 1.9$)
Case 20	14	1.0	0.10	AOD > 0.4	($\rho = 2.23$)
		Differences in Dust AAOD			
Case 21	14	1.0	0.10	AOD > 0.4	(dust +20%)
Case 22	14	1.0	0.10	AOD > 0.4	(dust −20%)

[a]Differences from the base case are given in parentheses.

with the largest 8 year average sensitivity value H_{ijk} are given in Figure 5.

[27] Two additional variables are required before the filter is applied. The first, Q_k, is a measure of the uncertainty associated with the model itself. For this case here, it is assumed to be 10% of the prior state covariance estimate at time $k = 0$, $\mathbf{P_o}$ (which is equal to $\mathbf{x}_{j,0}{}^T \times \mathbf{x}_{j,0}$, where T is a transpose operator). This assumption is further explored in the sensitivity runs section. The second is a matrix responsible for updating the emissions from one time step to the next, $\mathbf{M}_k$, which in this work is a unit matrix, since the emissions are treated as time invariant. Given that $\mathbf{M}_k$ is a unit matrix in this work, it has no impact on the filter equations and hence will not be considered further.

[28] The Kalman Filter (equations (5a)–(5d)) is then applied in sequence for each of the 96 monthly observations available. The first part of the filter (equation (5a)) describes that the forecast state covariance estimate $\mathbf{P}^f_k$ is updated by summing together the prior state covariance estimate $\mathbf{P}^a{}_{k-1}$ (the posterior from the previous time step) and the model error $\mathbf{Q}_{k-1}$. Physically, this is just stating that the state covariance estimate (error) is increase by the model error at each step. Note that the superscript a represents the filter step while f represents the step before the filter step.

$$\mathbf{P}^f{}_k = \mathbf{P}^a{}_{k-1} + \mathbf{Q}_{k-1} \tag{5a}$$

[29] The second stage of the filter defines the Kalman gain matrix, $\mathbf{K}_k$. This represents a balance between the error in the measurements, $\mathbf{R}_k$, and the sensitivity in the model's ability to predict how a change in emissions from region j will impact the respective variable i at the measurement's location, $\mathbf{H}_{ijk}{}^*\mathbf{P}^f{}_k{}^*\mathbf{H}_{ijk}{}^T$. Large values of the measurement error $\mathbf{R}_k$ or a high model sensitivity to the respective change in a given variable as a function of emissions, $\mathbf{H}_{ijk}{}^*\mathbf{P}^f{}_k{}^*\mathbf{H}_{ijk}{}^T$, imply that $\mathbf{K}_k$ will be smaller. This will then provide a lower probability for the present state to be updated or influenced by the observational data of interest. Note that $\mathbf{R}_k = \boldsymbol{\varepsilon}_k{}^T * \boldsymbol{\varepsilon}_k$ is a diagonal matrix, where $\boldsymbol{\varepsilon}_k$ is the vector containing some quantification of the measurement error at all measurement locations, for each time step k. Note that $^{-1}$ is the matrix inversion operator.

$$\mathbf{K}_k = \mathbf{P}^f{}_k{}^*\mathbf{H}_{ijk}{}^T{}^*\left(\mathbf{H}_{ijk}{}^*\mathbf{P}^f{}_k{}^*\mathbf{H}_{ijk}{}^T + \mathbf{R}_k\right)^{-1} \tag{5b}$$

[30] The third step in the filter process is updating the present state of the system with the measurement data. This involves the difference between the measurement $\mathbf{y}_{i0}$ and the model value at the point of the measurement $\mathbf{y}_{ik}$ and multiplying this difference by the Kalman gain matrix, $\mathbf{K}_k$. If the Kalman gain matrix is large (i.e., the measurement error and the model representation error of the state are both small), then greater significance will be placed on the measurement. Similarly, if the measurement error or the model representation error is large, then the Kalman Gain is small, and the added value of the new observation is not very significant. Finally, the larger the difference between the measurement and the model, the

Table 3. A Priori and a Posteriori (Optimized) BC Emissions by Region[a]

Region	1	2	3	4	5	6	7	8	9	Global
A priori	1.14	1.26	1.04	3.51	1.68	(1.89)	(1.19)	1.93	(0.73)	14.37
Base	1.03	1.39	1.19	3.67	2.10	3.62	1.73	1.90	1.21	17.83
Differences in a Priori *Emissions*										
Case 1	0.96	1.30	1.11	3.44	1.97	3.39	1.62	1.78	1.13	16.70
Case 2	1.05	1.42	1.21	3.76	2.15	3.71	1.77	1.94	1.24	18.27
Case 3	1.07	1.45	1.24	3.83	2.19	3.78	1.81	1.98	1.26	18.60
Differences in Interpolation Error										
Case 4	1.09	1.47	1.26	3.89	2.22	3.84	1.83	2.01	1.28	18.89
Case 5	1.03	1.39	1.18	3.66	2.10	3.61	1.73	1.89	1.21	17.79
Case 6	1.11	1.50	1.28	3.97	2.27	3.92	1.87	2.05	1.31	19.29
Case 7	1.13	1.53	1.30	4.03	2.31	3.98	1.90	2.08	1.33	19.61
Differences in Model Error										
(Case 8)	(0.87)	(1.18)	(1.00)	(3.10)	(1.77)	(3.06)	(1.46)	(1.60)	(1.02)	(15.07)
Case 9	1.00	1.34	1.15	3.55	2.03	3.50	1.67	1.83	1.17	17.24
Case 10	1.05	1.42	1.21	3.74	2.14	3.70	1.77	1.93	1.23	18.20
Case 11	1.07	1.44	1.23	3.80	2.17	3.75	1.79	1.96	1.25	18.46
Differences in the AERONET Cutoff										
Case 12	0.91	1.24	1.05	3.26	1.86	3.22	1.54	1.68	1.07	15.84
Case 13	0.85	1.14	0.97	3.01	1.72	2.97	1.42	1.56	0.99	14.63
Differences in SSA Assumptions of MBS										
Case 14	1.01	1.37	1.17	3.61	2.06	3.56	1.70	1.86	1.19	17.53
Case 15	1.03	1.39	1.19	3.68	2.10	3.63	1.73	1.90	1.21	17.87
Differences in BC Density										
Case 16	0.88	1.19	1.01	3.13	1.79	3.09	1.48	1.62	1.03	15.21
Case 17	1.28	1.73	1.47	4.56	2.61	4.50	2.15	2.35	1.50	22.15
Differences Using a Much Higher BC Density										
Case 18	1.43	(1.94)	1.65	(5.11)	2.92	(5.04)	(2.41)	2.64	1.68	(24.83)
(Case 19)	(1.74)	(2.35)	(2.00)	(6.20)	(3.55)	(6.12)	(2.92)	(3.20)	(2.04)	(30.13)
(Case 20)	(1.99)	(2.69)	(2.29)	(7.09)	(4.06)	(7.00)	(3.35)	(3.66)	(2.34)	(34.46)
Different Dust AAOD Values										
Case 21	0.97	1.31	1.12	3.46	1.98	3.42	1.63	1.79	1.14	16.82
Case 22	1.18	1.60	1.36	4.21	2.41	4.16	1.99	2.18	1.39	20.48

[a]Note that values in parentheses are outside the uncertainty range of the base value, even in the sensitivity cases (see Table 2).

more added value that the measurement carries, in terms of updating the state.

$$\mathbf{x}^a{}_{jk} = \mathbf{x}^a{}_{j,k-1} + \mathbf{K}_k{*}(\mathbf{y}^{\mathbf{o}}{}_{ik} - \mathbf{y}_{ik}) \tag{5c}$$

[31] The final step in the filter is updating the model covariance estimate. As can be seen, the model covariance estimate is decreased at each time step through two different factors. The first factor leading to the decrease in the model covariance is that when there is a high Kalman gain, $\mathbf{K}_k$, there is a low measurement error, thus implying that the measurement will have a large influence on the state and provide useful information to the update. The second is when the model is particularly sensitive to a measurement, $\mathbf{H}_{ijk}$, from a specific region, which implies that even if the gain is small, that it is still more relevant to reducing the uncertainty of the model state. Note that $\mathbf{I}$ is the identity matrix.

$$\mathbf{P}^a{}_k = \left(\mathbf{I} - \mathbf{K}_k{*}\mathbf{H}_{ijk}\right){*}\mathbf{P}^f{}_k \tag{5d}$$

[32] Alternatively, the procedures described in equations (4a) and (4b) could be replaced with a least square regression, a nonlinear least squares regression, or a three-dimensional variational data assimilation (3DVAR) approach. An obvious benefit of using the Kalman Filter compared to least square regression is that it is a series of best fits, continuously updated with new information at each time step. For example, in this paper, the Kalman Filter technique updates itself 96 times, one per month, for 8 years and therefore captures the nonlinearity of the response between a change in emissions in and the measured values of AAOD as a 96-piecewise linear approximation would, which is far better than a least squares fit, which is equivalent to a single tangent. Although a nonlinear least squares or other nonlinear-optimized regression may be able to take care of outliers and offer a possibly better fit, they also do not take into account the temporal variability in the field. As demonstrated in the example above, such temporal information provides a much better way to fit a nonlinear response. In this way, this method does not only provide a best fit for any given time step but instead will converge to the value sought by constantly minimizing the error with each update in the time series. And while a 3DVAR approach can take into account the temporal variability in the field, its performance relies upon the data being of high to excellent quality, with both the measurements and underlying model being assumed to be perfect, as any errors in the measurements or model will propagate through the system [e.g., *Courtier et al*., 1994; *Wergen*, 1992]. Given the large amount of uncertainty associated with the measurements used for BC, it is not certain whether a 3DVAR approach would even converge or not, with the reason being that data are required at each time step, otherwise uniform errors are generated which then cannot be quantified, and thus, these errors propagate through the system. Studies such as *Houtekamer et al*. [2005] and *Whitaker et al*. [2008] show that for global meteorological models with respect to assimilation of meteorological data, the Kalman Filter method works out better. Therefore, a further advantage of the Kalman Filter technique is that it quantifies the uncertainty of the estimate due to errors present in both the measurements and the model and therefore allows the end user to know the quantity of the contribution of the

Table 4. BC Emissions Uncertainties (Tg/yr) by Region

Region	1	2	3	4	5	6	7	8	9	Global
Error	0.32	0.44	0.37	1.16	0.66	1.14	0.54	0.60	0.38	5.63
Differences in a Priori *Emissions*										
Case 1	0.25	0.33	0.28	0.87	0.50	1.24	0.41	0.45	0.29	4.24
Case 2	0.35	0.47	0.40	1.25	0.71	1.23	0.59	0.64	0.41	6.06
Case 3	0.37	0.50	0.43	1.32	0.76	1.30	0.62	0.68	0.44	6.42
Differences in Interpolation Error										
Case 4	0.34	0.46	0.39	1.21	0.69	1.19	0.57	0.62	0.40	5.87
Case 5	0.25	0.34	0.29	0.90	0.52	1.29	0.43	0.47	0.30	4.39
Case 6	0.37	0.49	0.42	1.30	0.74	1.28	0.61	0.67	0.43	6.33
Case 7	0.39	0.52	0.45	1.38	0.79	1.36	0.65	0.71	0.46	6.71
Differences in Model Error										
Case 8	0.10	0.13	0.11	0.34	0.20	0.34	0.16	0.18	0.11	1.67
Case 9	0.28	0.38	0.33	1.01	0.58	1.00	0.48	0.52	0.33	4.91
Case 10	0.35	0.47	0.40	1.25	0.71	1.23	0.59	0.64	0.41	6.06
Case 11	0.37	0.50	0.42	1.31	0.75	1.30	0.62	0.68	0.43	6.38
Differences in the AERONET Cutoff										
Case 12	0.34	0.46	0.39	1.22	0.70	1.20	0.58	0.63	0.40	5.93
Case 13	0.30	0.41	0.35	1.09	0.62	1.07	0.51	0.56	0.36	5.28
Differences in SSA Assumptions of MBS										
Case 14	0.32	0.43	0.37	1.14	0.65	1.13	0.54	0.59	0.38	5.55
Case 15	0.32	0.44	0.37	1.15	0.66	1.14	0.54	0.60	0.38	5.60
Differences in BC Density										
Case 16	0.29	0.39	0.33	1.03	0.59	1.02	0.49	0.53	0.34	5.02
Case 17	0.37	0.50	0.43	1.33	0.76	1.31	0.63	0.69	0.44	6.45
Differences Using a Much Higher BC Density										
Case 18	0.40	0.54	0.46	1.43	0.82	1.41	0.67	0.74	0.47	6.94
Case 19	0.45	0.61	0.52	1.61	0.92	1.59	0.76	0.83	0.53	7.82
Case 20	0.49	0.66	0.56	1.74	1.00	1.72	0.82	0.90	0.56	8.47
Different Dust AAOD Values										
Case 21	0.32	0.43	0.36	1.13	0.65	1.11	0.53	0.58	0.37	5.48
Case 22	0.34	0.45	0.39	1.20	0.69	1.18	0.57	0.62	0.40	5.82

model error to the a posteriori state. This allows for the usefulness of each of the measurement to be determined and provides information on which component of the system is contributing the most to this uncertainty [*Enting*, 2002; *Prinn*, 2004].

2.4. Base Experimental Setup

[33] To successfully run the filter, a set of filter, model, and measurement variables and uncertainties needs to be defined. These values are chosen so that they are as representative as possible. Specifically, we have included the initial emissions estimate as ($\Sigma(\mathbf{x}_{j,0}) = 14$ Tg/yr) [*Wang*, 2004; *Cohen et al*., 2011]. To compute AAOD and $\mathrm{AAOD_{surf}}$ from the model results, we have used the values of mass density (ρ) and single-scattering albedo (ω) of BC taken from *Kim et al*. [2008]. The measurement error of interpolated data points is set to be 100% of the measurement value, or $\boldsymbol{\varepsilon}_k = 1.0\mathbf{y}^{\mathbf{o}}{}_{ik}$; the model error is 10% or $\mathbf{Q}_k = 0.1\mathbf{P}_k$, and station data is only included from AERONET stations if the corresponding AOD is greater than or equal to 0.4. These values are outlined as the base case in Table 2. The a priori values and results of the Kalman Filter, both region-by-region as well as the global totals, are given in Table 3. The uncertainty bands computed from the square root of the diagonal elements of $\mathbf{P}_k$ for the base case, region-by-region, are given in Table 4.

3. Results

3.1. Main Experiment

[34] We find that this method converges when the results are annually averaged in time, showing that the time series of data points used for the filter are sufficiently long enough to obtain a mathematically precise optimization. As is shown in Figures 6 and 7, the error bars are gradually decreasing around an annually varying cycle, which is shown by the fact that the 12 month running average value is not changing after the first 4 to 5 years worth of the analysis procedure. The convergence of the optimized emissions and associated uncertainty band, over the sequence of the Kalman Filter application to each data point, is shown in Figure 6 for the global total and in Figure 7 for each of the nine regions. A comparison between our global total top-down optimized emissions values (including uncertainty range), those from our a priori and those from other works, is given in Table 5. The net global results show that the optimized annual average values, even at the lowest value found by subtracting the uncertainty range from the optimized value, is still larger than those corresponding to various bottom-up methods [*Bond et al*., 2004; *Zhang et al*., 2009; *Lei et al*., 2011] as well as those adopted by the Intergovernmental Panel on Climate Change (IPCC) [*Moss et al*., 2010]. The only case where this is not true is our own a priori [*Wang*, 2004; *Kim et al*., 2008], which at about 14 Tg/yr is still lower than the optimized global value but is within the error range. When looking at the results on a region-by-region basis, we see that five regions have an optimized value quite different from their a priori, with Region 1 having an optimized emissions value lower and Regions 5, 6, 7, and 9 higher than the a priori. However, only Regions 6, 7, and 9 have an a posteriori that falls outside the range of the a priori plus and minus the error.

[35] We also find that there is a large month-to-month variation in the optimization. Since we have assumed that the emissions are time invariant, this month-to-month variation is due to factors unrelated to seasonal variation of emissions [e.g., *Cooke et al*., 2002; J. Cohen, in preparation, 2013],

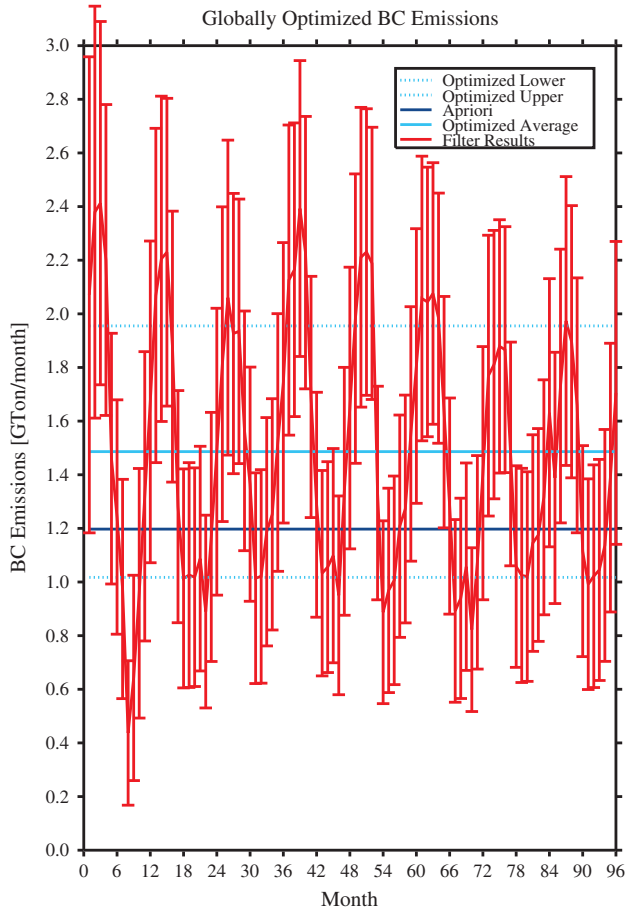

Figure 6. Annual average global-optimized emissions for the base inversion, with uncertainty bands, a priori average annual emissions, and the optimization sequence for the global BC emissions given by the Kalman Filter as it assimilates each data point.

which are not considered in this paper, and the time-varying information contained within the observations. This is partially due to temporal changes in the sensitivity matrix and partially due to variation in the observations of BC AAOD. For example, even in this context where we assume constant emissions, it is already demonstrated that there is a time-varying component of the column BC AAOD, as explained by *Cohen et al*. [2011]. Besides the seasonality of rainfall, this is also related to how the aging of BC leads to significant changes in its size, optical properties, and lifetime, and that this aging is strongly controlled by the season of the year, through its connection with sulfuric acid availability. Although it is expected that time variation of emissions will also contribute to this phenomenon, especially over certain regions of the world where seasonal fires occur, this is not explicitly considered in this analysis. A comparison between the annual average AAOD computed from our global total top-down optimized emissions values, including uncertainty range, the AAOD computed from our a priori, and those from other works is given in Table 6.

3.2. Sensitivity Experiments

[36] To ensure that these results are robust, we have recomputed the Kalman Filter results under many different conditions (Table 2). The first set of sensitivity tests addresses the suitability of the Kalman Filter equation initial conditions. The second set of tests addresses the impact of broadening the uncertainty associated with interpolated data points. The third set looks into the impact of general model errors and how they propagate and compare with measurement errors. The fourth set addresses the critical issue of the measurement unreliability of AAOD when the AERONET AOD is below 0.4. The fifth set focuses on uncertainties in terms of relating how black carbon interacts with radiation and absorption. The last set tests the sensitivity of optimized BC emissions to the uncertainty in dust AAOD. The results of the Kalman Filter for the sensitivity tests are given in Table 3, while the associated uncertainty bands for the sensitivity cases are given in Table 4.

[37] The first set of sensitivity tests are designed to see how changes in the initial emissions used for the Kalman Filter impact the optimized results. Since the optimized value of emissions is considerably larger than the a priori emissions of 14 Tg/yr, two higher values were selected. In Case 2, a value of $\Sigma(\mathbf{x}_{jk,0}) = 17$ Tg/yr was used, and in Case 3, a value of $\Sigma(\mathbf{x}_{jk,0}) = 20$ Tg/yr was used. Although starting with a higher initial value leads to a slightly higher optimized emission, it is only a very small change, always less than 5% of the original value, whether on the global total or a region-by-region basis. Furthermore, to compare against the commonly used a priori values that are around 8 Tg/yr, a further lower value was selected, and these results are shown in Case 1. Here starting with a lower initial value leads to a slightly lower optimized emission, but it is again only a very small change, always less than 10% of the original value. These changes are small compared with the error bounds and are not significant statistically. The reason for the higher (or lower) optimized values is that since the starting emission is at a higher (or lower) value, the values at the next time step are higher (or lower) as the filter steps forward. However, the results rapidly converge within the first year in all cases (except for the low case, where it takes roughly 4 years of time), leading to the minor end impact.

[38] The second set of sensitivity tests looks into the impact of broadening the uncertainty associated with interpolated data points on the optimized results. In these cases, the measurement error of all climatologically averaged and interpolated data points is set to 200% of the measurement value, or $\boldsymbol{\varepsilon}_k = 2.0\mathbf{y}^{\mathbf{o}}_k$. This effectively causes these data points to carry almost no weight in filter step 5c. These results are shown as Case 4 when $\Sigma(\mathbf{x}_{j,0}) = 14$ Tg/yr, Case 5 when $\Sigma(\mathbf{x}_{j,0}) = 8$ Tg/yr, Case 6 when $\Sigma(\mathbf{x}_{j,0}) = 17$ Tg/yr, and Case 7 when $\Sigma(\mathbf{x}_{j,0}) = 20$ Tg/yr. The first thing to observe from these results is that by weighting these values less, there is a roughly 1 Tg/yr increase in all of the optimized emissions results. The second thing is that the error range has increased by just fewer than 5% as compared to the base cases. These changes are in fact small compared with the error bounds from the base case and are not statistically significant. One rationale for this across the board increase in the optimized emissions as compared with the base value is that there might be bias toward lower AAOD values during months in which the data are not available. The slight increase in the error bounds also is consistent, since increasing the measurement error overall leads to a larger $\mathbf{R}_k$ value.

[39] A third set of sensitivity tests addresses the impact of general model errors, as represented via the Kalman Filter

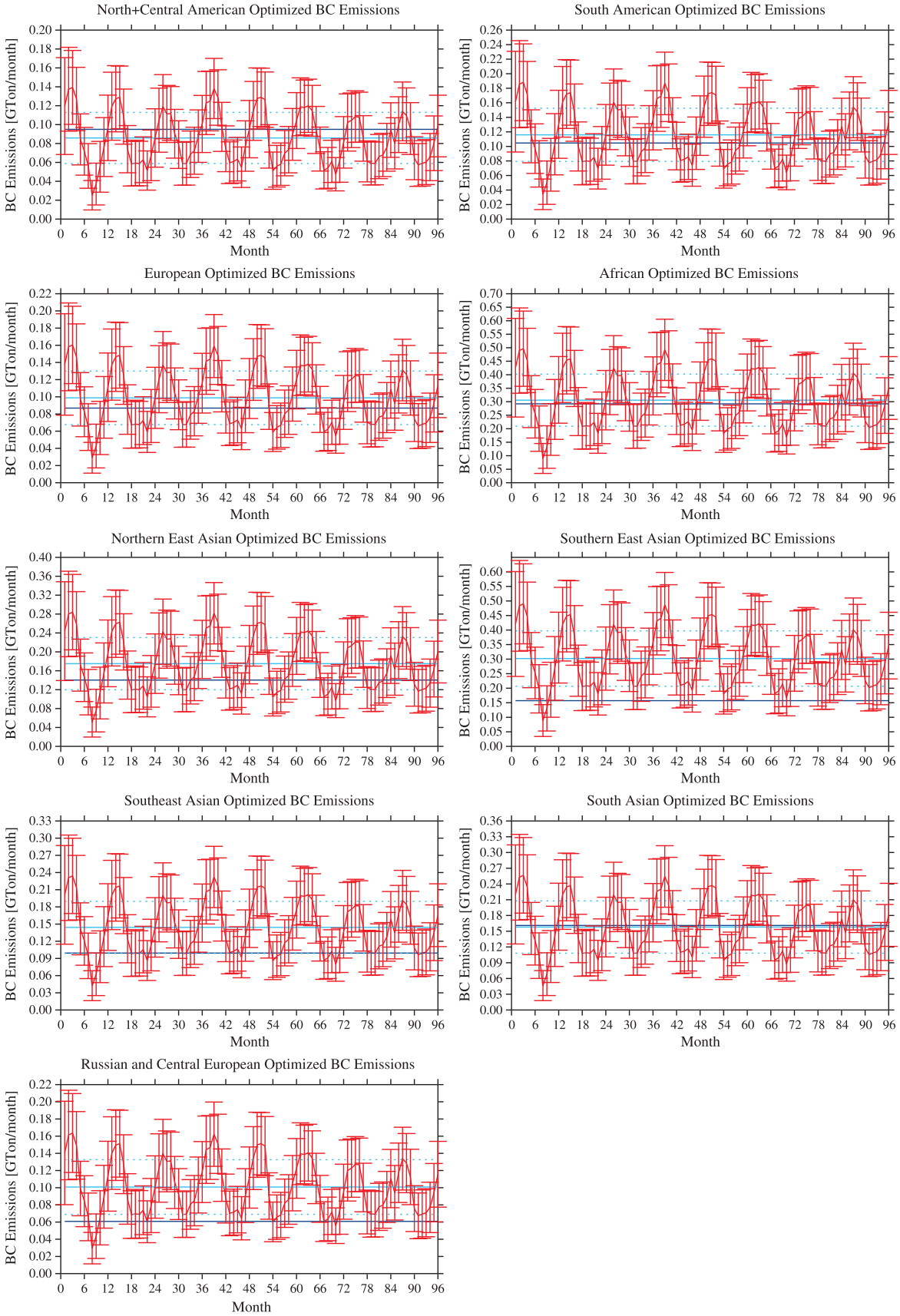

Figure 7. Annual average optimized emissions for the base inversion, by region (see Figure 4), with uncertainty bands, a priori average annual emissions, and the optimization sequence for the BC emissions given by the Kalman Filter as it assimilates each data point.

Table 5. Summary of Global Total BC Emissions From This Current Work as Well as Other Works Found in the Literature (Tg/yr)

	Global Emissions (Tg/yr)	Uncertainty Range (Tg/yr)
This work	17.8	12.2–23.4
A priori [*Wang*, 2004; *Cohen et al*., 2011]	14.4	None Given
Bond [*Bond et al*., 2004]	7.95	4.7–19.8 or 4.3–22
IPCC representative concentration pathways [*Van der Werf et al*., 2006; *Bond et al*., 2007]	7.662	7.662–8.800

equations. In these cases, the value for $\mathbf{Q}_k$ is defined as 0% (or perfect) in case 8, 5% in case 9, 15% in case 10, and 20% in case 11. There are two effects of increasing model error: first, the weighting of measurements is made to be more important, and second, the impact of the sensitivity matrix is weaker. Conversely, the opposite is true when there is a decrease in model error. The single most important result is that when model error is 0%, the estimated emissions are 2.6 Tg/yr lower than the base case, with a rapid rise in the a posteriori as the model error is increased. However, the majority of this increase occurs when the model error is increased from 0% to 5%, with subsequent 5% increases in model error leading to increasingly small increases in a posteriori. The second corresponding observation is that the error bound is extremely small in the case of 0% model error and that the error bound rises rapidly with the first increase from 0% to 5% model error (an increase of 3.4 Tg/yr). Subsequent 5% increases in model error lead to a considerably smaller increase in uncertainty bound. Third, it is important to point out that in reality the model is not perfect and that therefore some model error should exist. Given this point, it seems that just applying a small amount of model error, even just 5%, is already sufficient to find that the measurement values are indicative of a higher amount of emissions than the model itself allows for, when not considering model error. Finally, even in the case of 0% model error, all of the results are still found to lie within the error range given by the base case results.

[40] The next set of sensitivity tests attempts to examine the impact of the measurement unreliability caused by the lack of AAOD retrievals when AERONET AOD is below 0.4. This is addressed in two different manners. In Case 12, only the subset of AERONET stations that have at least 80% of their total data points with an AOD greater than 0.4 is considered. Therefore, this addresses the issue of how much a low bias in a large fraction of data points might influence the emissions estimate. In Case 13, a different data-processing technique from the one used by the AERONET program is applied to level 1 AERONET data to obtain AAOD values (S. Kinne, personal communication, 2011). In this case, the value of ω is also computed, even when the AOD is smaller than 0.4. Specifically, it treats ω in these cases as being exactly equal to the case where AOD equals 0.4, therefore fixing the AAOD to AOD ratio and in turn yielding a value for the AAOD. Notice that this method is different from those that the AERONET stations currently use. The results show that the emissions are considerably lower in Case 12, at 15.8 Tg/yr (which is 2.0 Tg/yr lower than the base value), and even slightly lower yet in Case 13, at 14.6 Tg/yr (which is 3.2 Tg/yr lower than the base value). However, these values still fall within the range given in the base case. One reason why Case 12 behaves this way is because the error range is now wider. A second possible reason is that some stations have more variability in their concentration levels, where often quite high values are recorded during certain times of the year but not during others. If these stations happen to have very high values only 1 or 2 months a year, such as those downwind from seasonal biomass burning, then they will be excluded, since they do not meet the 20% threshold in terms of the time series average, and hence, a bias may be introduced. Otherwise, if they meet the minimum 20% threshold (for example have 3 or 4 months of sufficiently high AAOD), since this procedure assumed that the emissions are annually averaged, the computed emissions will be an annualized average of these values, showing a high bias during certain months and a low bias during other months. With respect to Case 13, it is possible that assuming ω for low AOD conditions really does constrain the system, by providing far more information under cleaner conditions. However, since aerosols under different AOD levels at the same location likely have different chemical ages, this assumption may not be accurate. Furthermore, it is important to point out that two additional factors about the data set used in Case 13, as compared with AERONET Level 2 Data. First, the overall AOD values from this data set tend to be slightly lower than the same stations in AERONET Level 2 Data (the 2003 annual average AAOD from the Case 13 data is different from the AERONET data at 58 sites, with the maximum, average, and minimum difference of 0.04, 0.01, and −0.03, respectively), even when considering all measurements. Second, the seasonal variability is not the same. Perhaps there is a significant difference in how the inversions were done that merits further investigation.

[41] The next four sensitivity tests are focused on two important uncertainties in terms of relating how black carbon aerosol interacts with radiation, and hence the impact on particulate absorption. The first two of these cases examine the effect of placing a minimum on ω of aged black carbon (core-shell structured BC-sulfate mixture MBS only, not external BC) of 0.5 for Case 14 and a maximum value on ω of aged black carbon of 0.5 for Case 15 on aged black carbon. This corresponds to the values currently computed by the model, of a mixing ratio of roughly 15% sulfate in the mixed form of MBS, and which can be found in detail in *Kim et al*.

Table 6. Summary of Annual Average Anthropogenic Component of AAOD Computed Based on this Work and Others Found in the Literature ($\mathrm{AAOD} \times 10^{-3}$)

	AAOD ($\times 10^{-3}$)	Uncertainty Range ($\times 10^{-3}$)
This work: Global average	8.3	5.9–11
This work: 30°S to 0°N average	6.9	5.1–9.1
This work: 0°N to 30°N average	16	11–21
This work: 30°N to 60°N average	11	8.5–16
A priori [*Cohen et al*., 2011]	10.7	None given
Chung [*Chung et al*., 2012]	9.5	8.0–10
Chin [*Chin et al*., 2009]	8.6	None given

[2008, Figure 3]. The latter two cases look at the impacts of mass density, ρ, on the optical properties of black carbon, using a lower value of $\rho = 0.84$ g/cm^3 for Case 16 and a higher value of $\rho = 1.27$ g/cm^3 for Case 17. The first finding is that the limitations of ω seem to have little effect. The second finding is that changes in ρ seem to have a large effect; the decreased value of ρ (case 16) yields an optimal value of 15.2 Tg/yr (which is 2.6 Tg/yr lower than the base value), while the increased value of ρ (case 17) yields an optimal value of 22.2 Tg/yr (which is 4.3 Tg/yr higher than the base value). The optimized values in both of these cases still fall within the bounds of the base case. However, the spread between these two extremes is quite large, with these two results falling outside of the bound of error of each other. The reason for this is that the value of how strongly black carbon absorbs directly influences the AAOD. This is due to the fact that the mass extinction coefficient inversely varies with the density, as is born out in the results. However, an increase of density of 27% (Case 17) led to an increase in emissions of 24%, and a decrease in density of 16% (Case 16) led to a decrease in emissions of 15%. This shows that the direct linear scaling in density (and hence mass absorption efficiency) leads to a less than linear response in emissions. The small changes in emissions based on limiting ω are more interesting. It is possible that at the stations of interest, the total amount of aged black carbon has ω slightly under 0.5, which is why Case 14 had a larger effect, but that the actual ω was not significantly different from 0.5. A final possibility is that the quantity of sulfate in MBS, which in turn controls ω, does not vary substantially as a function of the emissions of BC, but perhaps more so for other species not explored in this paper such as SO_2, and hence, the mixing state is not that very sensitive to perturbations in BC emissions. This is a potentially interesting point to be explored in further work.

[42] A further set of cases look into the impacts of using even higher values than used in Case 17 for the mass density of BC, ρ, on the optical properties of black carbon. The density of external BC is assumed to be roughly 1 g/cm^3 in our model; however, *Bond and Bergstrom* [2006] and *Schuster et al*. [2005] recommend a considerably higher value. Specific cases tested include values ranging from the low end given by *Schuster et al*. [2005] of $\rho = 1.5$ g/cm^3 (Case 18), to the value recommended as ideal by *Bond and Bergstrom* [2006] of $\rho = 1.9$ g/cm^3 (Case 19), to the maximum value given by *Schuster et al*. [2005] of $\rho = 2.23$ g/cm^3 (Case 20). As expected from the results in Case 17, the optimized emissions calculated for Cases 18–20 are each respectively higher than the base case and that this increase is larger for higher values of ρ. Respectively, these optimized values are 24.8 Tg/yr (which is 7 Tg/yr higher than the base value), 30.1 Tg/yr (which is 12.3 Tg/yr higher than the base value), and 34.5 Tg/yr (which is 16.7 Tg/yr higher than the base value). It is interesting to note that again, the percentage increase in the optimized emissions, respectively, 39%, 69%, and 94%, continues to increase slower than the percentage increase in the value of ρ, respectively, 50%, 90%, and 123%. This indicates that the Kalman Filter method is indeed accounting for some of the higher-order nonlinearity in the response to this linear change in the extinction coefficient.

[43] The final set of sensitivity tests involves the AAOD of dust. Since this is an important component of the overall AAOD over certain regions of the world, any uncertainty in the dust absorption may impact on the value of the absorption associated with BC in or near those regions. To test this, two additional runs have been performed: one increases the AAOD of dust by 20% everywhere (Case 21), and the other decreases the AAOD of dust by 20% everywhere (Case 22). As can be observed from the results, Case 21 has a decrease in optimized emissions of about 1 Tg/yr, while Case 22 has an increase in optimized emissions of about 2.7 Tg/yr. While these results are not statistically significant and are further less important than some of the other tested sensitivity inputs, the response is a bit different. In this case, an increase in dust AAOD seems to have a considerably smaller impact on BC emissions than a same-sized decrease in dust AAOD. It is also important to note that the most heavily dust-laden areas, Africa, Northern East Asia, and India, optimized BC emissions do not particularly change in a different manner than other regions due to these changes made in dust AAOD. This suggests that sites heavily influenced by dust have little impact on our inversion. The changes in dust AAOD are more sensitive for regions that are only moderately or lightly impacted by dust in the first place. This result actually demonstrates that our data selection procedure is quite successful in avoiding the heavy dust regions. On the other hand, a decrease in dust AAOD requires a considerably larger increase in BC to offset, possibly due to the fact that the source regions of the dust and BC are from different locations. This result further shows that the impact of uncertainty in dust is also likely not too important unless its current AAOD is strongly overestimated.

[44] In conclusion, all of the sensitivity tests performed generate a spread of optimized emissions values but always still lying within the range of the base case. The only exception is the case for extremely high values of ρ, in which case the emissions lie above the range of the base case. Furthermore, we have identified that the mass density of black carbon, ρ, as it relates to optical absorption, is the most important sensitive parameter, while data error and constraints, and model error, also play an important role.

4. Discussion and Conclusions

[45] It is interesting to consider the reasons why the optimized emissions for Eastern Europe, Southern East Asia, and Southeast Asia are all significantly higher than the a priori, as displayed in Figure 8. The a priori in turn is already significantly higher than emissions values commonly found in the literature. In addition to these statistically significant cases, there are two borderline cases. The optimized value from Northern East Asia is higher than the a priori, while the optimized value from North and Central America is lower than the a priori. However, both of these results are not outside the boundaries of the optimized value and therefore are not statistically significantly different.

[46] In the case of East Asia, it is well documented that BC is consistently underpredicted by current bottom-up emissions inventories. Three possible factors for this are explained by assumptions used for generating the a priori: the economic growth in China has been consistently underpredicted by the MIT Emissions Predictions and Policy Analysis (EPPA) model [*Sokolov et al*., 2009] between 2000 and 2010; the locations of major cities on the coasts have been modeled with populations lower than their

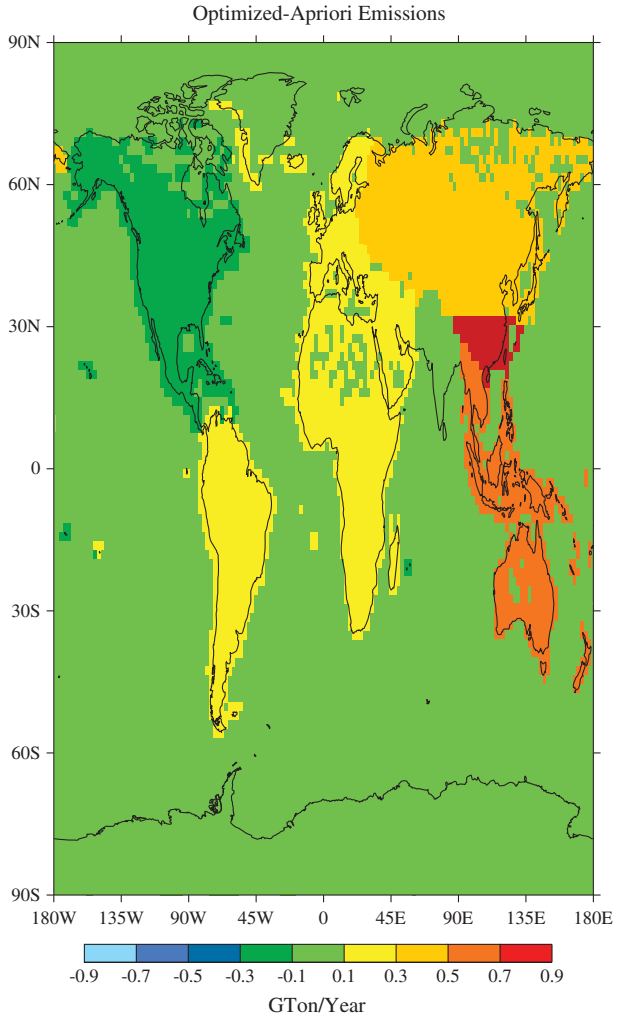

Figure 8. Difference between the region-by-region total base case posteriori and a priori emissions.

actual values by the EPPA model, since movement of people from interior regions to these coastal cities was not accounted for in terms of the population contribution of the emissions inventory; and that certain large emissions sources were completely missing, in both the EPPA a priori and in other cases [*Zhang et al*., 2009]. All three of these would lead to a systematic low emissions bias, as well as possibly an improper distribution. This third point is a possible reason why Northern East Asia was not completely outside the bounds while Southern East Asia was, since there are possibly agricultural sources of biomass burning in the South which are more prevalent than in the drier north; something that the a priori emissions estimates did not account for. This is further corroborated by the fact that there is no obvious bias in either the locations of the measurements in and downwind from these regions or in corresponding sensitivity matrix elements corresponding to these regions. This point is further supported by the addition of surface station measurements, which again are mostly influenced by local emissions in the two parts of East Asia, respectively.

[47] For the case of Southeast Asia, similarly to China, there has been a growing increase in economic activity and urbanization as well as a large migration of people from rural areas to those of the economic activity. This is confirmed by the fact that the EPPA model has consistently underpredicted the economic activity for Vietnam and Indonesia, from 2000 to 2010. A similar case of economic models underestimating activity in East Asia is a cause of the a priori being underestimated too. Given both of these examples, the fact that the a priori is underestimated is reasonable. This region has a reasonable number of stations to provide adequate spatial coverage, and no obvious bias in either the measurements or sensitivity matrix, therefore increasing the likelihood that these factors are not what is contributing to the large fractional increase in emissions due to the optimization process. However, the fact that a large amount of BC in this area is due to biomass burning, which is thus temporally variable while the emissions were assumed to be temporally invariant, could introduce some error into the inversion over this region [*Jeong and Wang*, 2010]. While this is an important potential contribution deserving of further study, this effort is focused on the annual average emissions.

[48] The case of Eastern Europe and Russia is more similar to that of East Asia, with the particular focus being on economic growth tending to be underestimated by the emissions prediction models. There is also no obvious bias among the stations in this region nor any obvious low or high value of the sensitivity matrix in this area. Furthermore, some of the European surface stations are located in this area and therefore provide a higher level of local certainty, similarly to the East Asia case.

[49] In the case of North and Central America, the inclusion of surface stations has led to a less negative estimation. Before including the surface stations, the optimal estimation of emissions was even lower than what it is found to be after the inclusion of these stations. This is because this region has one of the highest values of the sensitivity matrix for any region, there are few other measurements covering the northwestern and central portions of North America, and the error associated with these surface measurements is generally smaller than that with the AERONET measurements. Therefore, any reduction in the error term introduced to the sensitivity calculation should lead to greater numerical certainty, causing the value to be more reliable. The surface measurement terms help to offset this, since their impact almost exclusively impacts local emissions estimates.

[50] The final interesting case is the result for South Asia. In the case of South Asia, there are two special factors involved that may leave the result further open to investigation. First of all, a single AERONET station has an extremely high sensitivity value compared with the others for a given region, contributing $65 \pm 30\%$ to the total sensitivity matrix associated with the region. Therefore, the optimization is heavily dependent on this one station's result. Because of this, any bias or error in this station's data will heavily impact the result. Second, the two stations in South Asia have a far lower mean AAOD than those in the other regions and are both located in more remote sites, possibly leading to a bias. Furthermore, there are multiple surface and column measurements [*Lawrence and Lelieveld*, 2010] showing that BC concentrations and column loadings are higher than those predicted based on the a priori emissions. Therefore, it is hoped that as access to more stations in the outflow of the emissions sources over South Asia come online and as they

become more representative of the geographical locations in South Asia, this discrepancy can be resolved.

[51] In conclusion, we have introduced a Kalman Filter method, using BC AAOD measurements from AERONET, ground surface measurements from the EUSAAR, CAWNET, and NOAA networks, and the state-of-the-art MIT AERO-URBAN model, as a means of optimizing for the emissions of BC aerosol. Our results, the first in the literature to use this method to produce a global top-down estimation of the emissions of BC aerosol, lead to an optimized value of 17.8 ± 5.6 Tg/yr. This result is far larger than the bottom-up estimates currently used in the majority of global aerosol modeling efforts. It is hoped that this work will open the door to further efforts to better quantify and reduce the uncertainty of the emissions of primary aerosol species so that the ultimate uncertainty of the impact that aerosols play on global- and regional-scale climate systems can be minimized.

[52] **Acknowledgments.** This work was supported by the Singapore National Research Foundation (NRF) through a grant to the Center for Environmental Sensing and Monitoring (CENSAM) of the Singapore-MIT Alliance for Research and Technology (SMART), by the U.S. National Science Foundation (AGS-0944121), US DOE (DE-FG02-94ER61937), US EPA (XA-83600001-1), and by the Singapore MOE's AcRF Tier 1 grant (R-302-000-062-133). The authors want to thank all of the principal investigators of AERONET, EUSAAR, CAWNET, and NOAA stations for making the data available, Sang-Woo Kim for his help in obtaining and interpreting the CAWNET data, Stefan Kinne for providing an additional and separate inversion of AERONET station data, Natalie Mahowald for providing the dust climatology data, and Phillip Rasch for his help in setting up the atmospheric transport mode of the CAM3.1 model. Many constructive comments and suggestions from Tami Bond and several other anonymous reviewers helped enhance the manuscript.

References

Bond, T. C., D. G. Streets, K. F. Yarber, S. M. Nelson, J. H. Woo, and Z. Klimont (2004), A technology-based global inventory of black and organic carbon emissions from combustion, *J. Geophys. Res.*, *109*, D14203, doi:10.1029/2003JD003697.

Bond, T. C., and R. W. Bergstrom (2006), Light absorption by carbonaceous particles: An investigative review, *Aerosol Sci. Technol.*, *40*, 27–67.

Bond, T. C., E. Bhardwaj, R. Dong, R. Jogani, S. Jung, C. Roden, D. G. Streets, S. Fernandes, and N. Trautmann (2007), Historical emissions of black and organic carbon aerosol from energy-related combustion, 1850–2000, *Global Biogeochem. Cycles*, *21*, GB2018, doi:10.1029/2006GB002840

Cavalli, F., M. Vianna, K. E. Tyyri, J. Genberg, and J. P. Putaud (2010), Toward a standardized thermal-optical protocol for measuring atmospheric organic and elemental carbon: The EUSAAR protocol, *Atmos. Meas. Tech.*, *3*, 79–89.

Chen, Y. H., and R. G. Prinn (2006), Estimation of atmospheric methane emissions between 1996 and 2001 using a three-dimensional global chemical transport model, *J. Geophys. Res. 111*, D10307, doi:10.1029/2005JD006058.

Chin, M., T. Diehl, O. Dubovik, T. F. Eck, B. N. Holben, A. Sinyuk, and D. G. Streets (2009), Light absorption by pollution, dust, and biomass burning aerosols: A global model study and evaluation with AERONET measurements, *Ann. Geophys.*, *27*, 3439–3464.

Chung, C. E., and V. Ramanathan (2003), South Asian haze forcing: Remote impacts with implications to ENSO and AO, *J. Clim.*, *16*(11), 1791–1806.

Chung, S. H., and J. H. Seinfeld (2005), Climate response of direct radiative forcing of anthropogenic black carbon, *J. Geophys. Res.*, *110*, D11102, doi:10.1029/2004JD005441

Chung, C. E., V. Ramanathan, and D. Decremer (2012), Observationally constrained estimates of carbonaceous aerosol radiative forcing, *Proc. Natl. Acad. Sci. U.S.A.*, doi:10.1073/pnas.1203707109.

Cohen, J. B., and R. G. Prinn (2011), Development of a fast, urban chemistry metamodel for inclusion in global models, *Atmos. Chem. Phys.*, *11*, 7629–7656, doi:10.5194/acp-11-7629-2011.

Cohen, J. B., R. G. Prinn, and C. Wang (2011), The impact of detailed urban-scale processing on the composition, distribution, and radiative forcing of anthropogenic aerosols, *Geophys. Res. Lett.*, *38*, L10808, doi:10.1029/2011GL047417.

Collins, W. D., et al. (2006), The Community Climate System Model Version 3 (CCSM3), *J. Clim.*, *19*(11), 2,122–2,143, doi:10.1175/JCLI3761.1.

Cooke, W. F., V. Ramaswamy, and P. Kasibhatla (2002), A general circulation model study of the global carbonaceous aerosol distribution, *J. Geophys. Res.*, *107*(D16), 4279, doi:10.1029/2001JD001274.

Courtier, P., J. N. Thepaut, and A. Hollingsworth (1994), A strategy for operational implementation of 4D-Var, using an incremental approach, *Q. J. R. Meteor. Soc.*, *120*, 1,367–1,387.

Delene, D. J., and J. A. Ogren (2002), Variability of aerosol optical properties at four North American surface monitoring sites, *J. Atmos. Sci.*, *59*(6), 1135–1150.

Dubovik, O., A. Smirnov, B. N. Holben, M. D. King, Y. J. Kaufman, T. F. Eck, and I. Slutker (2000), Accuracy assessments of aerosol optical properties retrieved from Aerosol Robotic Network (AERONET) Sun and sky radiance measurements, *J. Geophys. Res.*, *105*(D8), 9,791–9,806.

Enting, I. G. (2002), *Inverse Problems in Atmospheric Constituent Transport*, Cambridge Univ. Press, New York.

Forster, P., et al. (2007), Changes in atmospheric constituents and in radiative forcing, in *Climate Change 2007: The Physical Science Basis. Contribution of Working Group I to the Fourth Assessment Report of the Intergovernmental Panel on Climate Change*, edited by S. Solomon et al., pp. 129–234, Cambridge Univ. Press, Cambridge, United Kingdom and New York, NY, USA.

Hakami, A., D. K. Henze, J. H. Seinfeld, T. Chai, Y. Tang, G. R. Carmichael, and A. Sandu (2005), Adjoint inverse modeling of black carbon during the Asian Pacific Regional Aerosol Characterization Experiment, *J. Geophys. Res.*, *110*, D14301, doi:10.1029/2004JD005671.

Holben, B. N., et al. (1998), AERONET—A federated instrument network and data archive for aerosol characterization, *Remote Sens. Environ.*, *66*, 1–16.

Hoose, C., and O. Möhler (2012), Heterogeneous ice nucleation on atmospheric aerosols: A review of results from laboratory experiments, *Atmos. Chem. Phys.*, *12*, 9817–9854.

Houtekamer, P. L., H. L. Mitchell, G. Pellerin, M. Buehner, M. Charron, L. Spacek, and B. Hansen (2005), Atmospheric data assimilation with an ensemble Kalman filter: Results with real observations, *Mon. Weather Rev.*, *133*, 604–620.

Jacobson, M. Z. (2001), Strong radiative heating due to the mixing state of black carbon in atmospheric aerosols, *Nature*, *409*, 695–697.

Jacobson, M. Z. (2012), Investigating cloud absorption effects: Global absorption properties of black carbon, tar balls, and soil dust in clouds and aerosols, *J. Geophys. Res.*, *117*, D06205, doi:10.1029/2011JD017218.

Jeong, G. R., and C. Wang (2010), Climate effects of seasonally varying Biomass Burning emitted Carbonaceous Aerosols (BBCA), *Atmos. Chem. Phys.*, *10*, 8373–8389.

Kalman, R. E. (1960), A new approach to linear filtering and prediction problems, *Trans. ASME Ser. D*, *82*, 35–45.

Kalnay, E., et al. (1996), The NCEP/NCAR 40-year reanalysis project, *Bull. Am. Meteorol. Soc.*, *77*(3), 437–471.

Kim, D., C. Wang, A. M. L. Ekman, M. C. Barth, and P. J. Rasch (2008), Distribution and direct radiative forcing of carbonaceous and sulfate aerosols in an interactive size-resolving aerosol-climate model, *J. Geophys. Res.*, *113*, D16309, doi:10.1029/2007JD009756.

Kondo, Y., N. Oshima, M. Kajino, R. Mikami, N. Moteki, N. Takegawa, R. L. Verma, Y. Kajii, S. Kato, and A. Takami (2011), Emissions of black carbon in East Asia estimated from observations at a remote site in the East China Sea, *J. Geophys. Res.*, *116*, D16201, doi:10.1029/2011JD015637.

Lawrence, M. G., and J. Lelieveld (2010), Atmospheric pollutant outflow from southern Asia: A review, *Atmos. Chem. Phys.*, *10*, 11,017–11,096.

Lei, Y., Q. Zhang, K. B. He, and D. G. Streets (2011), Primary anthropogenic aerosol emission trends for China, 1990–2005, *Atmos. Chem. Phys.*, *11*, 931–954, doi:10.5194/acp-11-931-2011.

Mahowald, N. M., R. G. Prinn, and P. J. Rasch (1997), Deducing CCI3F emissions using an inverse method and chemical transport models with assimilated winds, *J. Geophys. Res.*, *102*(D23), 28,153–28,168.

Mahowald, N., C. Luo, J. Corral, and C. S. Zender (2003), Interannual variability in atmospheric mineral aerosols from a 22-year model simulation and observational data, *J. Geophys. Res.*, *108*(D12), 4352, doi:10.1029/2002JD002821.

Ming, Y., V. Ramaswamy, and G. Persad (2010), Two opposing effects of absorbing aerosols on global-mean precipitation, *Geophys. Res. Lett.*, *37*, L13701, doi:10.1029/2010GL042895.

Moss, R. H., et al. (2010), The next generation of scenarios for climate change research and assessment, *Nature*, *463*, 747–756, doi:10.1038/nature08823.

Prinn, R. G. (2004), Measurement equation for trace chemicals in fluids and solution of its inverse, in inverse methods in global biogeochemical cycles, *Geophys. Monogr. Ser.*, *114*, 3–18, doi:10.1029/GM114p0003.

Prinn, R. G., et al. (2001), Evidence for substantial variations of atmospheric hydroxyl radicals in the past two decades, *Science*, *292*, 1,882.

Ramanathan, V., and G. Carmichael (2008), Global and regional climate changes due to black carbon, *Nat. Geosci.*, *1*, 221–227.

Ramanathan, V., P. J. Crutzen, J. T. Kiehl, and D. Rosenfeld (2001), Aerosols, climate, and the hydrological cycle, *Science*, *294*, 2119–2124.

Ramanathan, V., C. E. Chung, D. Kim, T. Bettge, L. Buja, J. T. Kiehl, W. M. Washington, Q. Fu, D. R. Sikka, and M. Wild (2005), Atmospheric brown clouds: Impacts on South Asian climate and hydrological cycle, *Proc. Natl. Acad. Sci. U.S.A.*, *102*, 5326–5333, doi:10.1073/pnas.0500656102.

Satheesh, S. K., and V. Ramanathan (2000), Large differences in tropical aerosol forcing at the top of the atmosphere and Earth's surface, *Nature*, *405*, 60–63.

Sato, M., J. Hansen, D. Koch, A. Lacis, R. Ruedy, O. Dubovik, B. Holben, M. Chin, and T. Novakov (2003), Global atmospheric black carbon inferred from AERONET, *Proc. Natl. Acad. Sci. U.S.A.*, *100*, 6319–6324, doi:10.1073/pnas.0731897100.

Schuster, G. L., O. Dubovik, B. Holben, and E. Clothiaux (2005), Inferring black carbon content and specific absorption from Aerosol Robotic Network (AERONET) aerosol retrievals, *J. Geophys. Res.*, *110*, D10S17, doi:10.1029/2004JD004548.

Sokolov, A. P., P. H. Stone, C. E. Forest, R. Prinn, M. C. Sarofim, M. Webster, S. Paltsev, and C. A. Schlosser (2009), Probabilistic forecast for twenty-first century climate based on uncertainties in emissions (without policy) and climate parameters, *J. Clim.*, *22*(19), 5175–5204.

Sorenson, H. W. (1970), Least-squares estimation—From Gauss to Kalman, *IEEE Spectrum*, *7*(7), 63–68.

Tao, W.-K., J.-P. Chen, Z. Li, C. Wang, and C. Zhang (2012), Impact of aerosols on convective clouds and precipitation, *Rev Geophys*, *50*, RG2001, doi:10.1029/2011RG000369.

Tarantola, A., and B. Valette (1982), Generalized nonlinear inverse problems solved using the least squares criterion, *Rev. Geophys. Space Phys.*, *20*(2), 219–232.

Van der Werf, G., J. T. Randerson, L. Giglio, G. J. Collatz, P. S. Kasibhatla, and A. F. Arellano Jr. (2006), Interannual variability in global biomass burning emissions from 1997 to 2004, *Atmos. Chem. Phys.*, *6*, 3423–3441.

Wang, C. (2004), A modeling study on the climate impacts of black carbon aerosols, *J. Geophys. Res. 109*, D03106, doi:10.1029/2003JD004084.

Wang, C. (2009), The sensitivity of tropical convective precipitation to the direct radiative forcings of black carbon aerosols emitted from major regions, *Ann. Geophys.*, *27*, 3705–3711, doi:10.5194/angeo-27-3705-2009.

Wang, C., G. R. Jeong, and N. Mahowald (2009), Particulate absorption of solar radiation: Anthropogenic aerosols vs. dust, *Atmos. Chem. Phys.*, *9*, 3935–3945.

Wang, Q., et al. (2011), Sources of carbonaceous aerosols and deposited black carbon in the Arctic in winter-spring: Implications for radiative forcing, *Atmos. Chem. Phys.*, *11*, 12,453–12,473.

Wergen, W. (1992), The effect of model errors in variational assimilation, *Tellus*, *44A*, 297–313.

Whitaker, J. S., T. M. Hamill, X. Wei, Y. Song, and Z. Toth (2008), Ensemble data assimilation with the NCEP global forecast system, *Mon. Weather Rev.*, *136*, 463–482.

Yongtao H., M. T. Odman, and A. G. Russel (2009), Top-down analysis of the elemental carbon emissions inventory in the United States by inverse modeling using Community Multiscale Air Quality model with decoupled direct method (CMAQ-DDM), *J. Geophys. Res.*, *114*, D24302, doi:10.1029/2009JD011987.

Zhang, S., J. E. Penner, and O. Torres (2005), Inverse modeling of biomass burning emissions using Total Ozone Mapping Spectrometer aerosol index for 1997, *J. Geophys. Res.*, *110*, D21306, doi:10.1029/2004JD005738.

Zhang, Q., et al. (2009), Asian emissions in 2006 for the NASA INTEX-B mission, *Atmos. Chem. Phys.*, *9*, 5131–5153.

Zhang, X. Y., Y. Q. Wang, T. Niu, X. C. Zhang, S. L. Gong, Y. M. Zhang, and J. Y. Sun (2012), Atmospheric aerosol compositions in China: Spatial/temporal variability, chemical signature, regional haze distribution and comparisons with global aerosols, *Atmos. Chem. Phys.*, *12*, 779–799, doi:10.5194/acp-12-779-2012.

MIT JOINT PROGRAM ON THE SCIENCE AND POLICY OF GLOBAL CHANGE

REPRINT SERIES Recent Issues

Joint Program Reprints are available free of charge (limited quantities). To order: please use contact information on inside of front cover.

2013-25 Toward evaluating the effect of climate change on investments in the water resource sector: insights from the forecast and analysis of hydrological indicators in developing countries, Strzepek, K., M. Jacobsen, B. Boehlert and J. Neumann, *Environmental Research Letters*, 8(4): 044014 (2013)

2013-26 Modeling water resources within the framework of the MIT Integrated Global System Model: IGSM-WRS, Strzepek, K., A. Schlosser, A. Gueneau, X. Gao, É. Blanc, C. Fant, B. Rasheed and H.D. Jacoby, *Journal of Advances in Modeling Earth Systems*, 5(3): 638–653 (2013)

2013-27 Economic and emissions impacts of renewable fuel goals for aviation in the US, Winchester, N., D. McConnachie, C. Wollersheim and I.A. Waitz, *Transportation Research Part A: Policy and Practice*, 58(2013):116–128 (2013)

2013-28 An integrated assessment modeling framework for uncertainty studies in global and regional climate change: the MIT IGSM-CAM (version 1.0), Monier, E., J.R. Scott, A.P. Sokolov, C.E. Forest and C.A. Schlosser, *Geosci. Model Dev.* 6: 2063–2085 (2013)

2013-29 Characterization of the wind power resource in Europe and its intermittency, Cosseron, A., U.B. Gunturu and C.A. Schlosser, *Energy Procedia*, 40(2013): 58–66 (2013)

2013-30 Climate Change and Emissions Impacts on Atmospheric PAH Transport to the Arctic, Friedman, C.L., Y. Zhang and N.E. Selin, *Environmental Science & Technology*, online first, doi: 10.1021/es403098w (2013)

2013-31 Cost Concepts for Climate Change Mitigation, Paltsev, S. and P. Capros, *Climate Change Economics*, 4(Suppl.1): 1340003 (2013)

2013-32 Insights and issues with simulating terrestrial DOC loading of Arctic river networks, Kicklighter, D.W., D.J. Hayes, J.W. McClelland, B.J. Peterson, A.D. McGuire and J.M. Melillo, *Ecological Applications*, 23(8): 1817–1836 (2013)

2013-33 A Contemporary Carbon Balance for the Northeast Region of the United States, Lu X., D.W. Kicklighter, J.M. Melillo, P. Yang, B. Rosenzweig, C.J. Vörösmarty, B. Gross and R.J. Stewart, *Environmental Science & Technology*, 47(3): 13230–13238 (2013)

2013-34 European-Led Climate Policy versus Global Mitigation Action: Implications on Trade, Technology, and Energy, De Cian, E., I. Keppo, J. Bollen, S. Carrara, H. Förster, M. Hübler, A. Kanudia, S. Paltsev, R.D. Sands and K. Schumacher, *Climate Change Economics*, 4(Suppl. 1): 1340002 (2013)

2013-35 Beyond 2020—Strategies and Costs for Transforming the European Energy System, Knopf, B., Y.-H.H. Chen, E. De Cian, H. Förster, A. Kanudia, I. Karkatsouli, I. Keppo, T. Koljonen, K. Schumacher, D.P. van Vuuren, *Climate Change Economics*, 4(Suppl. 1): 1340001 (2013)

2013-36 Estimating regional methane surface fluxes: the relative importance of surface and GOSAT mole fraction measurements, Fraser, B., P.I. Palmer, L. Feng, H. Boesch, A. Cogan, R. Parker, E.J. Dlugokencky, P.J. Fraser, P.B. Krummel, R.L. Langenfelds, S. O'Doherty, R.G. Prinn, L.P. Steele, M. van der Schoot and R.F. Weiss, *Atmospheric Chemistry and Physics*, 13: 5697–5713 (2013)

2013-37 The variability of methane, nitrous oxide and sulfur hexaflouride in Northeast India, Ganesan, A.L., A. Chatterjee, R.G. Prinn, C.M. Harth, P.K. Salameh, A.J. Manning, B.D. Hall, J. Mühle, L.K. Meredith, R.F. Weiss, S. O'Doherty and D. Young, *Atmospheric Chemistry and Physics*, 13: 10633–10644 (2013)

2013-38 Integrated economic and climate projections for impact assessment, Paltsev, S., E. Monier, J. Scott, A. Sokolov and J.M. Reilly, *Climatic Change*, October 2013, doi: 10.1007/s10584-013-0892-3 (2013)

2014-1 Estimating a global black carbon emissions using a top-down Kalman Filter approach, Cohen, J.B. and C. Wang, *Journal of Geophysical Research—Atmospheres*, 119: 1–17, doi: 10.1002/2013JD019912 (2014)

For a complete list of titles see:
http://globalchange.mit.edu/research/publications/reprints

MIT Joint Program on
The Science and Policy of Global Change
Massachusetts Institute of Technology
77 Massachusetts Avenue, E19-411
Cambridge, MA 02139
USA